10-2013

The non-linear dynamics of electromagnetically actuated microbeam resonators with purely parametric excitations

Jeffrey F. Rhoads
Birck Nanotechnology Center, Purdue University, jfrhoads@purdue.edu

Vijay Kumar
Birck Nanotechnology Center, Purdue University

Steven W. Shaw
Michigan State University

Kimberly L. Turner
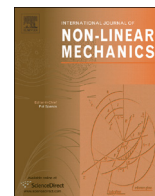*University of California - Santa Barbara*

The non-linear dynamics of electromagnetically actuated microbeam resonators with purely parametric excitations

CrossMark

Jeffrey F. Rhoads [a,b,c,*], Vijay Kumar [a,b,c], Steven W. Shaw [d], Kimberly L. Turner [e]

[a] School of Mechanical Engineering, Purdue University, West Lafayette, IN 47907, United States
[b] Ray W. Herrick Laboratories, Purdue University, West Lafayette, IN 47907, United States
[c] Birck Nanotechnology Center, Purdue University, West Lafayette, IN 47907, United States
[d] Department of Mechanical Engineering, Michigan State University, East Lansing, MI 48824, United States
[e] Department of Mechanical Engineering, University of California, Santa Barbara, Santa Barbara, CA 93106, United States

ARTICLE INFO

ABSTRACT

Electromagnetic micro-transducers have been utilized in a number of distinct applications in recent years due, in large part, to their scalability, low power consumption, self-sensing capabilities and ease of integration with external hardware. In the present work, the highly non-linear dynamic behavior of a new class of parametrically excited, electromagnetically actuated microcantilevers is explored. The system is modeled using classical energy methods and its frequency response behavior is subsequently characterized using perturbation methods and bifurcation analysis. The recovered results provide a clear understanding of the effects of fifth-order non-linearities in a parametrically excited microresonator, and are currently guiding experimental work on electromagnetically actuated oscillators and microresonator arrays.

1. Introduction

Electromagnetic micro-transducers have garnered increasing interest in recent years due to their high scalability, low power consumption, self-sensing capabilities and ease of integration with on-chip hardware elements [1–5]. While such devices were initially proposed for use in radio frequency (rf) signal filters [6], the successful realization of Lorentz force actuation and magnetomotive-based sensing in simple micro- and nanostructures has led to a rapid technological expansion. Today electromagnetically actuated (EMA) microsystems are being exploited in a variety of applications ranging from charge detectors to micro- and nano-positioners (see, for example [7–15]).

The present work examines the highly non-linear behavior of a new class of parametrically excited EMA microcantilevers, which is believed to have significant potential in a variety of applications, including resonant mass sensing and electromechanical signal processing. These devices, previously introduced in Refs. [16–19] and shown in Fig. 1, consist of a single silicon microcantilever with two current loops deposited on the resonator's surface. The resonator is actuated electromagnetically using a Lorentz force, which is generated by the interaction between an external permanent magnet and the integrated current loop, and sensed using an

induced electromotive force (emf), which results from the movement of the integrated current loop through the magnetic field.

Given that the utility of the EMA microcantilevers detailed herein is largely limited by the predictability of their non-linear behaviors, the work begins with the systematic modeling of the large amplitude motions of a representative device using classical beam theory. The resulting distributed-parameter system model is then systematically reduced to a comparatively simpler lumped-mass model, which is analyzed using perturbation techniques. Plausible system behaviors believed to be useful for the stated applications are subsequently examined, and the work concludes with a brief review of the work's findings and a summary of on-going and planned research. It should be noted that the results presented herein, though developed with EMA microdevices in mind, are amenable to a variety of parametrically excited cantilever systems, the analyses of which rarely, if ever, consider the effects of non-linear parametric excitations (notable exceptions are Refs. [20,21]).

2. Formulation of a distributed-parameter model

Given that the electromagnetically actuated microcantilevers of interest here have been shown (in experiments) to exhibit moderately large response amplitudes near parametric resonance, the distributed-system model used to capture their dynamic behavior must allow for large elastic deformations [16]. As such,

* Corresponding author.
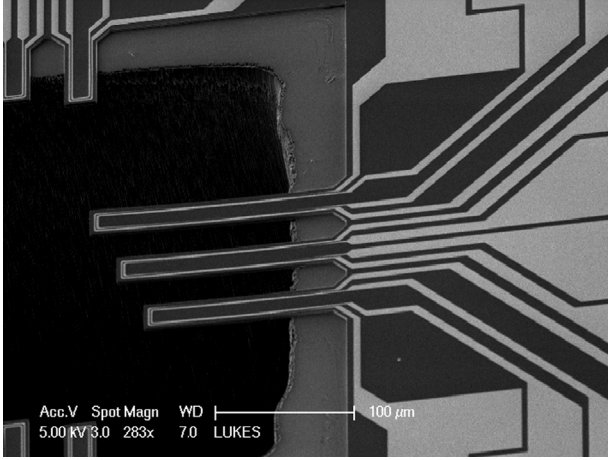 E-mail address: jfrhoads@purdue.edu (J.F. Rhoads).

Fig. 1. Representative electromagnetically-actuated microcantilever. The microcantilever is comprised of two independent current loops, one for actuation and another for sensing [22].
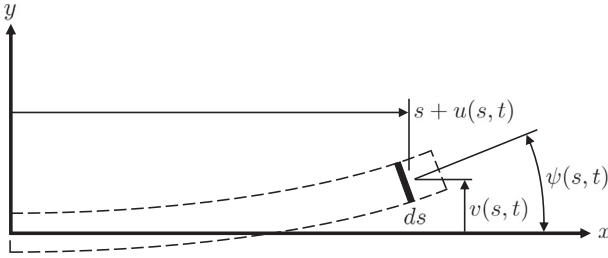

Fig. 2. Beam element with variable descriptions.

the non-linear, energy-based approach introduced in Refs. [23,24] and subsequently revisited in Ref. [25] is adopted here.

Assuming that the microbeam resonators of interest are uniform and have negligible rotational inertias, the specific Lagrangian of a given resonator can be approximated by

$$\overline{L} = \tfrac{1}{2} m(\dot{u}^2 + \dot{v}^2) - \tfrac{1}{2} D(\psi')^2, \tag{1}$$

where m and D represent the device's specific mass and flexural stiffness, respectively (see Fig. 2). Noting this, and further assuming that the neutral axis of the beam is inextensible, and thus that

$$(1 + u')^2 + (v')^2 = 1, \tag{2}$$

results in a governing variational equation for the system, derived from extended Hamilton's principle, given by

$$\delta H = 0 = \delta \int_{t_1}^{t_2} \int_0^l \left\{ \overline{L} + \frac{1}{2} \lambda [1 - (1 + u')^2 - (v')^2] \right\} ds\, dt$$
$$+ \int_{t_1}^{t_2} \int_0^l (Q_u \delta u + Q_v \delta v)\, ds\, dt, \tag{3}$$

where l and s represent the beam's total length and arc length variable, Q_u and Q_v represent the planar, non-conservative forces in the u and v directions, and λ represents a Lagrange multiplier introduced to maintain the inextensibility constraint. Integrating this equation by parts successively, while enforcing the kinematic constraint relating the Euler angle ψ to the planar displacements,

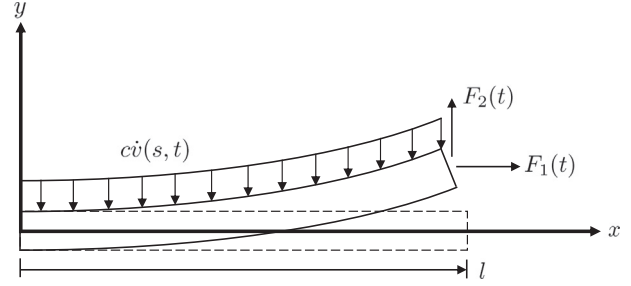$$\tan \psi = \frac{v'}{1 + u'}, \tag{4}$$

Fig. 3. Schematic of the beam with non-conservative force contributions.

yields the equations governing longitudinal and transverse dynamics, as well the system's boundary conditions

$$G_u' = \left[A_\psi \frac{\partial \psi}{\partial u'} + \lambda(1 + u') \right]' = m\ddot{u} - Q_u, \tag{5}$$

$$G_v' = \left[A_\psi \frac{\partial \psi}{\partial v'} + \lambda v' \right]' = m\ddot{v} - Q_v, \tag{6}$$

$$\{-G_u \delta u - G_v \delta v + H_u \delta u' + H_v \delta v'\}|_0^l = 0. \tag{7}$$

Note that here and throughout the remainder of the work, A_ψ, H_u, and H_v are given by

$$A_\psi = \frac{\partial^2 \overline{L}}{\partial t \partial \dot{\psi}} + \frac{\partial^2 \overline{L}}{\partial s \partial \psi'} - \frac{\partial \overline{L}}{\partial \psi}, \tag{8}$$

$$H_\varphi = \frac{\partial \overline{L}}{\partial \psi'} \frac{\partial \psi}{\partial \varphi'}, \quad \varphi = u, v. \tag{9}$$

In order to decouple Eqs. (5) and (6) and ultimately obtain a single equation of motion for the system, the Lagrange multiplier must be extracted from Eq. (5). To facilitate this, fifth-order Taylor series approximations[1] for both u and ψ, resulting from the kinematic and inextensibility constraints, are introduced, namely,

$$u(s, t) \approx -\frac{1}{2} \int_0^s (v')^2\, ds - \frac{1}{8} \int_0^s (v')^4\, ds, \tag{10}$$

$$\psi = v'\left(1 + \frac{(v')^2}{6} + \frac{3(v')^4}{40} + H.O.T.\right) \approx v' + \frac{(v')^3}{6} + \frac{3(v')^5}{40}. \tag{11}$$

Assuming ideal cantilever boundary conditions, specifically,

$$u(0, t) = 0, \quad v(0, t) = 0, \quad v'(0, t) = 0, \tag{12}$$

$$G_u(l, t) = 0 \quad G_v(l, t) = 0, \quad H_v - \frac{H_u v'}{1 + u'}\Big|_{s=l} = 0, \tag{13}$$

and that the longitudinal non-conservative force Q_u (see Fig. 3) can be accurately represented by a single point load applied at the endpoint of the beam (or more accurately an infinitesimal distance away—an idealization used here to avoid incorporating the force in the system's boundary conditions), defined by

$$Q_u = F_1(t)\delta(s - l), \tag{14}$$

where δ represent the Dirac delta function, results in an approximate Lagrange multiplier given by

$$\lambda \approx -Dv'v''' - D(v')^2(v'')^2 - D(v')^3 v''' - \frac{1}{2} m \int_l^s \frac{\partial^2}{\partial t^2} \int_0^s (v')^2\, ds\, ds$$
$$- \frac{1}{8} m \int_l^s \frac{\partial^2}{\partial t^2} \int_0^s (v')^4\, ds\, ds - \frac{1}{4} m(v')^2 \int_l^s \frac{\partial^2}{\partial t^2} \int_0^s (v')^2\, ds\, ds$$

---

[1] The experimental results presented in Ref. [16] indicate that fifth-order non-linearities are likely required to capture all of the experimental phenomena witnessed to date.

$$- \int_l^s F_1(t)\delta(s-l)\, ds - \frac{1}{2}(v')^2 \int_l^s F_1(t)\delta(s-l)\, ds$$

$$- \frac{3}{8}(v')^4 \int_l^s F_1(t)\delta(s-l)\, ds. \tag{15}$$

Substituting this value back into Eq. (6), defining the specific mass m and the flexural stiffness D according to

$$m = \rho A, \qquad D = EI, \tag{16}$$

where ρ, A, E, and I represent the device's mass density, cross-sectional area, Modulus of Elasticity, and cross-sectional moment of inertia, respectively, and further assuming that the transverse non-conservative force is given by

$$Q_v = F_2(t)\delta(s-l) - c\dot{v}, \tag{17}$$

where c represents the specific viscous damping coefficient, results in a fifth-order approximation of the system's equation of motion

$$\rho A \frac{\partial^2 v}{\partial t^2} + c \frac{\partial v}{\partial t} + EI \frac{\partial^4 v}{\partial s^4} + EI \left(\frac{\partial^2 v}{\partial s^2}\right)^3 + 4EI\left(\frac{\partial v}{\partial s}\right)\left(\frac{\partial^2 v}{\partial s^2}\right)\left(\frac{\partial^3 v}{\partial s^3}\right)$$

$$+ 6EI\left(\frac{\partial v}{\partial s}\right)^2\left(\frac{\partial^2 v}{\partial s^2}\right)^3 + 8EI\left(\frac{\partial v}{\partial s}\right)^3\left(\frac{\partial^2 v}{\partial s^2}\right)\left(\frac{\partial^3 v}{\partial s^3}\right)$$

$$+ EI\left(\frac{\partial v}{\partial s}\right)^2\left(\frac{\partial^4 v}{\partial s^4}\right) + EI\left(\frac{\partial v}{\partial s}\right)^4\left(\frac{\partial^4 v}{\partial s^4}\right)$$

$$+ \frac{1}{2}\rho A \frac{\partial^2 v}{\partial s^2} \int_l^s \frac{\partial^2}{\partial t^2} \int_0^s \left(\frac{\partial v}{\partial s}\right)^2 ds\, ds$$

$$+ \frac{1}{2}\rho A \frac{\partial v}{\partial s} \int_0^s \frac{\partial^2}{\partial t^2} \left(\frac{\partial v}{\partial s}\right)^2 ds + \frac{\partial^2 v}{\partial s^2} \int_l^s F_1(t)\delta(s-l)\, ds$$

$$+ \frac{\partial v}{\partial s} F_1(t)\delta(s-l) + \frac{1}{8}\rho A \frac{\partial^2 v}{\partial s^2} \int_l^s \frac{\partial^2}{\partial t^2} \int_0^s \left(\frac{\partial v}{\partial s}\right)^4 ds\, ds$$

$$+ \frac{1}{8}\rho A \frac{\partial v}{\partial s} \int_0^s \frac{\partial^2}{\partial t^2} \left(\frac{\partial v}{\partial s}\right)^4 ds$$

$$+ \frac{3}{4}\rho A \left(\frac{\partial v}{\partial s}\right)^2\left(\frac{\partial^2 v}{\partial s^2}\right) \int_l^s \frac{\partial^2}{\partial t^2} \int_0^s \left(\frac{\partial v}{\partial s}\right)^2 ds\, ds$$

$$+ \frac{1}{4}\rho A \left(\frac{\partial v}{\partial s}\right)^3 \int_0^s \frac{\partial^2}{\partial t^2} \left(\frac{\partial v}{\partial s}\right)^2 ds$$

$$+ \frac{3}{2}\left(\frac{\partial v}{\partial s}\right)^2\left(\frac{\partial^2 v}{\partial s^2}\right) \int_l^s F_1(t)\delta(s-l)\, ds$$

$$+ \frac{1}{2}\left(\frac{\partial v}{\partial s}\right)^3 F_1(t)\delta(s-l)$$

$$+ \frac{15}{8}\left(\frac{\partial v}{\partial s}\right)^4\left(\frac{\partial^2 v}{\partial s^2}\right) \int_l^s F_1(t)\delta(s-l)\, ds$$

$$+ \frac{3}{8}\left(\frac{\partial v}{\partial s}\right)^5 F_1(t)\delta(s-l)$$

$$= F_2(t)\delta(s-l). \tag{18}$$

To reduce the number of free parameters in this equation, a consistent scaling of the displacement and time variables is introduced. Specifically, the vertical displacement v and the arc length variable s are scaled by a characteristic displacement of the system v_0 (e.g. the beam's thickness or width) and undeformed length l, respectively, according to

$$\hat{v} = \frac{v}{v_0}, \quad \hat{s} = \frac{s}{l}, \tag{19}$$

and time is scaled by a characteristic period of the system T according to

$$\hat{t} = \frac{t}{T}, \tag{20}$$

where

$$T = \sqrt{\frac{\rho A l^4}{EI}}. \tag{21}$$

Introducing a new non-dimensional damping coefficient $\hat{c}$, defined by

$$\hat{c} = \frac{cT}{\rho A}, \tag{22}$$

and invoking the Dirac delta identity

$$\delta(ax) = \frac{1}{a}\delta(x), \quad a > 0 \tag{23}$$

reveals a scaled, distributed-parameter model for the system given by

$$\frac{\partial^2 \hat{v}}{\partial \hat{t}^2} + \hat{c}\frac{\partial \hat{v}}{\partial \hat{t}} + \frac{\partial^4 \hat{v}}{\partial \hat{s}^4} + \frac{v_0^2}{l^2}\left(\frac{\partial^2 \hat{v}}{\partial \hat{s}^2}\right)^3 + 4\frac{v_0^2}{l^2}\left(\frac{\partial \hat{v}}{\partial \hat{s}}\right)\left(\frac{\partial^2 \hat{v}}{\partial \hat{s}^2}\right)\left(\frac{\partial^3 \hat{v}}{\partial \hat{s}^3}\right)$$

$$+ \frac{v_0^2}{l^2}\left(\frac{\partial \hat{v}}{\partial \hat{s}}\right)^2\left(\frac{\partial^4 \hat{v}}{\partial \hat{s}^4}\right) + \frac{v_0^2}{2l^2}\frac{\partial \hat{v}}{\partial \hat{s}} \int_0^{\hat{s}} \frac{\partial^2}{\partial \hat{t}^2} \left(\frac{\partial \hat{v}}{\partial \hat{s}}\right)^2 d\hat{s}$$

$$+ \frac{v_0^2}{2l^2}\frac{\partial^2 \hat{v}}{\partial \hat{s}^2} \int_1^{\hat{s}} \frac{\partial^2}{\partial \hat{t}^2} \int_0^{\hat{s}} \left(\frac{\partial \hat{v}}{\partial \hat{s}}\right)^2 d\hat{s}\, d\hat{s} + \frac{l^2}{EI}\frac{\partial^2 \hat{v}}{\partial \hat{s}^2} \int_1^{\hat{s}} F_1(t)\delta(\hat{s}-1)d\hat{s}$$

$$+ \frac{l^2}{EI}\left(\frac{\partial \hat{v}}{\partial \hat{s}}\right)F_1(t)\delta(\hat{s}-1) + 6\frac{v_0^4}{l^4}\left(\frac{\partial \hat{v}}{\partial \hat{s}}\right)^2\left(\frac{\partial^2 \hat{v}}{\partial \hat{s}^2}\right)^3$$

$$+ 8\frac{v_0^4}{l^4}\left(\frac{\partial \hat{v}}{\partial \hat{s}}\right)^3\left(\frac{\partial^2 \hat{v}}{\partial \hat{s}^2}\right)\left(\frac{\partial^3 \hat{v}}{\partial \hat{s}^3}\right) + \frac{v_0^4}{l^4}\left(\frac{\partial \hat{v}}{\partial \hat{s}}\right)^4\left(\frac{\partial^4 \hat{v}}{\partial \hat{s}^4}\right)$$

$$+ \frac{v_0^4}{8l^4}\frac{\partial^2 \hat{v}}{\partial \hat{s}^2} \int_1^{\hat{s}} \frac{\partial^2}{\partial \hat{t}^2} \int_0^{\hat{s}} \left(\frac{\partial \hat{v}}{\partial \hat{s}}\right)^4 d\hat{s}\, d\hat{s} + \frac{v_0^4}{8l^4}\frac{\partial \hat{v}}{\partial \hat{s}} \int_0^{\hat{s}} \frac{\partial^2}{\partial \hat{t}^2} \left(\frac{\partial \hat{v}}{\partial \hat{s}}\right)^4 d\hat{s}$$

$$+ \frac{v_0^4}{4l^4}\left(\frac{\partial \hat{v}}{\partial \hat{s}}\right)^3 \int_0^{\hat{s}} \frac{\partial^2}{\partial \hat{t}^2} \left(\frac{\partial \hat{v}}{\partial \hat{s}}\right)^2 d\hat{s}$$

$$+ \frac{3v_0^4}{4l^4}\left(\frac{\partial \hat{v}}{\partial \hat{s}}\right)^2\left(\frac{\partial^2 \hat{v}}{\partial \hat{s}^2}\right) \int_1^{\hat{s}} \frac{\partial^2}{\partial \hat{t}^2} \int_0^{\hat{s}} \left(\frac{\partial \hat{v}}{\partial \hat{s}}\right)^2 d\hat{s}\, d\hat{s}$$

$$+ \frac{3v_0^2}{2EI}\left(\frac{\partial \hat{v}}{\partial \hat{s}}\right)^2\left(\frac{\partial^2 \hat{v}}{\partial \hat{s}^2}\right) \int_1^{\hat{s}} F_1(t)\delta(\hat{s}-1)d\hat{s}$$

$$+ \frac{v_0^2}{2EI}\left(\frac{\partial \hat{v}}{\partial \hat{s}}\right)^3 F_1(t)\delta(\hat{s}-1)$$

$$+ \frac{15v_0^4}{8EIl^2}\left(\frac{\partial \hat{v}}{\partial \hat{s}}\right)^4\left(\frac{\partial^2 \hat{v}}{\partial \hat{s}^2}\right) \int_1^{\hat{s}} F_1(t)\delta(\hat{s}-1)\, d\hat{s}$$

$$+ \frac{3v_0^4}{8EIl^2}\left(\frac{\partial \hat{v}}{\partial \hat{s}}\right)^5 F_1(t)\delta(\hat{s}-1)$$

$$= \frac{F_2(t)l^3}{v_0 EI}\delta(\hat{s}-1). \tag{24}$$

Though, theoretically, the behavior of the system can be directly recovered from this equation of motion, the practicality of this approach is questionable. As such, the model presented in Eq. (24) is used to develop a consistent lumped-mass model, which is amenable to analysis, as described in the following section.

3. Formulation of a lumped-mass model

To facilitate non-linear analysis and ultimately predictive design, the governing partial differential equation presented in Eq. (24) can be reduced to a system of non-linear ordinary differential equations through modal projection. Specifically, the dynamic variable $\hat{v}(\hat{s}, \hat{t})$ can be expanded using the system's mode shapes $\phi_i(\hat{s})$ according to

$$\hat{v}(\hat{s}, \hat{t}) = \sum_{i=1}^{\infty} w_i(\hat{t})\phi_i(\hat{s}). \tag{25}$$

Due to the dominance of first mode behavior in the experimental studies completed to date, a truncated, single-mode expansion proves sufficient for analysis, namely,

$$\hat{v}(\hat{s}, \hat{t}) = w(\hat{t})\phi(\hat{s}). \tag{26}$$

Given that the system's non-conservative forces and non-linearities are subsequently assumed to be 'small', the first assumed mode can be recovered using the linear differential equation

$$\phi^{iv} - \lambda^4 \phi = 0, \tag{27}$$

with boundary conditions

$$\phi(0) = 0, \quad \phi'(0) = 0, \quad \phi''(1) = 0, \quad \phi'''(1) = 0. \tag{28}$$

Though additional mode shapes could be included in the above expansion to increase the accuracy of the lumped-mass model, the slight improvement that results is largely negated by the added complexity of the analysis.

Prior to the final derivation of the EMA microbeam's lumped-mass model, it also proves convenient to expand the system's applied non-conservative forces in terms of physical parameters. As these forces (apart from a small contribution arising from viscous damping) result from the interaction between an external permanent magnet and a current loop integrated into the microbeam, they can be approximated using the Lorentz force model

$$\vec{F}(t) = i(t) \int d\vec{l} \times \vec{B}, \tag{29}$$

where $i(t)$, $d\vec{l}$, and $\vec{B}$ represent the current passing through the integrated loop, the length of a differential vector element of the loop, and the magnetic field, respectively. Assuming a two harmonic AC drive current with an additional DC component (which could be used for frequency tuning), the non-conservative force model can be represented as

$$\begin{aligned} \vec{F}(t) &= F_1(t)\mathbf{i} + F_2(t)\mathbf{j} \\ &= (i_{DC} + i_1 \cos \omega t + i_2 \cos 2\omega t)gB(\cos \alpha \mathbf{i} + \sin \alpha \mathbf{j}), \end{aligned} \tag{30}$$

where g represents the width of current loop and α specifies the orientation of the magnetic field (assumed to be uniform and unidirectional) with respect to a vertical reference (measured in the counterclockwise direction). Introducing this model, as well as the state variable expansion detailed above, into Eq. (24) and projecting the resulting equation back onto the first mode through the use of an inner product operator results in the final, lumped-mass equation of motion for the system

$$\begin{aligned} z'' &+ 2\varepsilon\zeta z' + (1 + \varepsilon\lambda_1 \cos \Omega\tau + \varepsilon\gamma_1 \cos 2\Omega\tau)z \\ &+ (\varepsilon\chi_3 + \varepsilon\lambda_3 \cos \Omega\tau + \varepsilon\gamma_3 \cos 2\Omega\tau)z^3 + \varepsilon\beta(z'^2 z + z^2 z'') \\ &+ (\varepsilon\chi_5 + \varepsilon\lambda_5 \cos \Omega\tau + \varepsilon\gamma_5 \cos 2\Omega\tau)z^5 + \varepsilon\nu_1 z^3 z'^2 + \varepsilon\nu_2 z^4 z'' \\ &= \varepsilon\eta_0 + \varepsilon\eta_1 \cos \Omega\tau + \varepsilon\eta_2 \cos 2\Omega\tau. \end{aligned} \tag{31}$$

System parameters are defined in Appendix A.

4. Derivation of the system's averaged equations

Though the equation of motion detailed in Eq. (31) is similar in form to those previously considered in Refs. [21,26–28], the addition of fifth-order non-linearities (which, as previously noted, are required to fully explain all of the system behaviors recorded to date) requires that the analysis of the non-linear, parametrically excited system be revisited. As this represents a non-trivial extension of prior work, the analysis contained herein begins anew, despite a partial overlap with results previously detailed in Refs. [27,28].

As devices with purely parametric excitations are likely to have the most desirable non-linear frequency response characteristics in practical application, the present study limits itself to the special case where the magnetic field is oriented in the vertical direction[2] ($\alpha = 0$). Accordingly, all of the direct forcing terms which appear in the system's equation of motion (i.e., $\eta_i = 0$, $i = 0, 1, 2$) are eliminated due to their dependence on $\sin \alpha$. Additionally, it should be noted that all non-linear, forcing, and damping parameters which appear in the parametrically excited system's equation of motion have been assumed to be 'small' (as denoted by the presence of the book-keeping parameter ε)–an assumption that is typically valid for MEMS resonators in lightly damped environments (see, for example, Ref. [28]).

To simplify analysis, a standard perturbation technique, the method of averaging, is employed. To facilitate this approach, a constrained coordinate transformation is first introduced into Eq. (31)

$$z(\tau) = a(\tau) \cos(\Omega\tau + \psi(\tau)), \tag{32}$$

$$z'(\tau) = -a(\tau)\Omega \sin(\Omega\tau + \psi(\tau)). \tag{33}$$

Additionally, to capture the system's near-resonant behavior, a frequency detuning parameter σ is introduced, defined by

$$\sigma = \frac{\Omega - 1}{\varepsilon}. \tag{34}$$

Separating the equations that result from substitution, in terms of amplitude and phase, and averaging over one period of the resonator's response ($2\pi/\Omega$) yields the pair of 'slow-flow' equations governing the system's behavior

$$a' = \tfrac{1}{64}a\varepsilon[-64\zeta + (16\gamma_1 + 8\gamma_3 a^2 + 5\gamma_5 a^4) \sin 2\psi] + \mathcal{O}(\varepsilon^2), \tag{35}$$

$$\begin{aligned} \psi' &= \tfrac{1}{64}\varepsilon[8a^2(3\chi_3 - 2\beta) + 4a^4(5\chi_5 + \nu_1 - 5\nu_2) - 64\sigma \\ &\quad + (16(\gamma_1 + a^2\gamma_3) + 15a^4\gamma_5) \cos 2\psi] + \mathcal{O}(\varepsilon^2). \end{aligned} \tag{36}$$

5. Steady-state system behaviors

With the averaged equations detailed above in hand, the system's steady-state behavior can be easily recovered by setting $(a', \psi') = (0, 0)$ and solving for the steady-state amplitudes and phases. Given that the system's non-linear behavior is of principal interest here and that this behavior is largely unaffected by damping, damping is assumed to be negligible ($\zeta = 0$). Those readers interested in the effects of small damping are referred to Ref. [28].

Adopting the above procedure reveals that the EMA microbeam has a trivial solution (with indeterminant phase) and four pairs of physically realizable, non-trivial solutions given, in terms of amplitude and phase, by

$$\overline{a}_1 = \pm 2\sqrt{\frac{-\nu_{3,1} + \sqrt{\nu_{3,1}^2 - \nu_{5,1}(\gamma_1 - 4\sigma)}}{\nu_{5,1}}}, \quad \overline{\psi}_1 = 0, \tag{37}$$

$$\overline{a}_2 = \pm 2\sqrt{\frac{-\nu_{3,1} - \sqrt{\nu_{3,1}^2 - \nu_{5,1}(\gamma_1 - 4\sigma)}}{\nu_{5,1}}}, \quad \overline{\psi}_2 = 0, \tag{38}$$

$$\overline{a}_3 = \pm 2\sqrt{\frac{-\nu_{3,2} + \sqrt{\nu_{3,2}^2 + \nu_{5,2}(\gamma_1 + 4\sigma)}}{\nu_{5,2}}}, \quad \overline{\psi}_3 = \frac{\pi}{2}, \tag{39}$$

---

[2] On-going work is aimed at predicting system responses for arbitrary α. Though this general case is expected to yield non-ideal system characteristics, a proper understanding of this case is requisite given that the orientation of the magnetic field may be hard to accurately specify in final device implementations.

$$\overline{a}_4 = \pm 2\sqrt{\frac{-\nu_{3,2} - \sqrt{\nu_{3,2}^2 + \nu_{5,2}(\gamma_1 + 4\sigma)}}{\nu_{5,2}}}, \quad \overline{\psi}_4 = \frac{\pi}{2}. \tag{40}$$

Note that each $\pm$ pair of solutions, as well as solutions with magnitude π phase shifts, represent the same physical response. Furthermore, note that here and throughout the remaining portions of this work ρ_3 and ρ_5 are used to represent the system's third- and fifth-order mechanical non-linearities (incorporating inertial terms), given by

$$\rho_3 = 3\chi_3 - 2\beta, \quad \rho_5 = 5\chi_5 + \nu_1 - 5\nu_2, \tag{41}$$

and $\nu_{3,1}$, $\nu_{3,2}$, $\nu_{5,1}$, and $\nu_{5,2}$ are used to represent the system's third- and fifth-order effective non-linearities, which are given by

$$\nu_{3,1} = \rho_3 + 2\gamma_3, \qquad \nu_{3,2} = \rho_3 - 2\gamma_3, \tag{42}$$

$$\nu_{5,1} = 4\rho_5 + 15\gamma_5, \qquad \nu_{5,2} = 4\rho_5 - 15\gamma_5. \tag{43}$$

Each of these parameters prove critical in characterizing the system's steady state behavior.

It is also worth noting that the system examined herein can have, providing certain parameter conditions are met, two additional constant-amplitude solution pairs with amplitudes given by

$$\overline{a}_5 = \pm \frac{2}{\sqrt{5}}\sqrt{\frac{-\gamma_3 + \sqrt{\gamma_3^2 - 5\gamma_1\gamma_5}}{\gamma_5}}, \tag{44}$$

$$\overline{a}_6 = \pm \frac{2}{\sqrt{5}}\sqrt{\frac{-\gamma_3 - \sqrt{\gamma_3^2 - 5\gamma_1\gamma_5}}{\gamma_5}}. \tag{45}$$

As these solutions are not realizable with the current device configurations, further discussion of these solutions is omitted. It is worth noting, however, that the addition of alternative transduction mechanisms or the use of non-uniform beam geometries may facilitate their appearance, which in turn can lead to significant changes in the system's qualitative behavior. Accordingly, care must be taken in the course of device design.

Before proceeding with a thorough examination of the system's qualitative behavior and its dependence on the third- and fifth-order effective non-linearities detailed above, it is prudent to briefly consider the local stability of the system's steady-state solutions. For present purposes, the local stability of the system can be determined by considering the linear behavior of the system's averaged equations near each of the system's steady-state solutions. Accordingly, by defining a composite state vector $X(\tau)$ according to

$$X(\tau) = \begin{bmatrix} a(\tau) \\ \psi(\tau) \end{bmatrix} \tag{46}$$

and a composite steady-state solution vector X^* according to

$$X^* = \begin{bmatrix} a^* \\ \psi^* \end{bmatrix}, \tag{47}$$

the local linearized equation of motion for the system can be rewritten as

$$Y'(\tau) = J(X^*)Y(\tau), \tag{48}$$

where $Y(\tau)$ represents the state's deviation from the steady state, that is

$$Y(\tau) = X(\tau) - X^*, \tag{49}$$

and J represents the Jacobian matrix of the averaged equations evaluated at the steady state. The stability of the various responses can now be directly deduced from the eigenvalues of the linearized system's Jacobian.

To simplify stability analysis, the system's eigenvalues can be characterized using the trace and determinant of the 2×2

Jacobian detailed above [29]. Specifically, the eigenvalues can be expressed in terms of the trace, T, and the determinant, Δ, as

$$\Lambda_{1,2} = \tfrac{1}{2}(T \pm \sqrt{T^2 - 4\Delta}). \tag{50}$$

For the undamped case under consideration here, the trace of the Jacobian for each of the steady-state responses is zero ($T=0$), and thus for non-trivial eigenvalues only two generic equilibrium types are possible, saddles (unstable) and centers (marginally stable), and the type of equilibrium that exists depends solely on the sign of the determinant Δ. Specifically, when $\Delta > 0$ the equilibrium is a center, and when $\Delta < 0$ the equilibrium is a saddle. The remaining case, $\Delta = 0$, corresponds to the degenerate case of two identically zero eigenvalues, and as such is used only to identify where stability changes occur.

Utilizing the criteria outlined above, the stability of the five solutions of interest (the trivial solution and the four physically consistent solution pairs) can be determined. In particular, it can be shown (with a conversion to Cartesian coordinates) that the trivial solution exists as a saddle point for all frequencies (detuning values) between σ_1 and σ_2, where

$$\sigma_{1,2} = \pm \frac{\gamma_1}{4}, \tag{51}$$

and as a center elsewhere. Similarly, a_1 and a_2 can be shown to have critical detuning values of σ_1 and σ_3, where

$$\sigma_3 = \frac{-\nu_{3,1}^2}{4\nu_{5,1}} + \frac{\gamma_1}{4}, \tag{52}$$

and a_3 and a_4 can be shown to have critical detuning values of σ_2 and σ_4, where

$$\sigma_4 = \frac{-\nu_{3,2}^2}{4\nu_{5,2}} - \frac{\gamma_1}{4}. \tag{53}$$

As each of these critical detuning values, as well as the sign of the Jacobian's determinant in between, is dependent on numerous system parameters, a number of distinct stability configurations exist. Rather than delineating each of these configurations here, the cases are detailed below as part of an examination of the system's frequency response.

6. Frequency responses

As evident from Eqs. (37)–(40), the qualitative behavior of the system detailed herein is not dependent on a single effective non-linearity, but rather a set of effective non-linearities, which collectively dictate the nature of the system response. In Ref. [28], the authors examined similar behavior in the context of a third-order, parametrically excited system using a simple parameter space investigation. Though a similar approach is adopted here, the addition of fifth-order non-linearities requires a hierarchical analysis.

Generally speaking, the third-order effective non-linearities detailed in Eq. (42) dictate the system's non-trivial behavior in the vicinity of the pitchfork bifurcations that occur at σ_1 and σ_2. In particular, selecting system parameters such that $\nu_{3,1} > 0$ and $\nu_{3,2} > 0$ results in a frequency response with third-order hardening characteristics and selecting $\nu_{3,1} < 0$ and $\nu_{3,2} < 0$ results in a frequency response with third-order softening characteristics. Clearly, under certain conditions, $\nu_{3,1}$ and $\nu_{3,2}$ can be selected to have opposite signs. Under these conditions the system exhibits 'mixed' non-linear characteristics, wherein the response curves initially bend away from one another.[3]

---

[3] Note that these curves would bend toward each other in the lower half-plane of the parameter space shown in Fig. 4. The response is significantly more
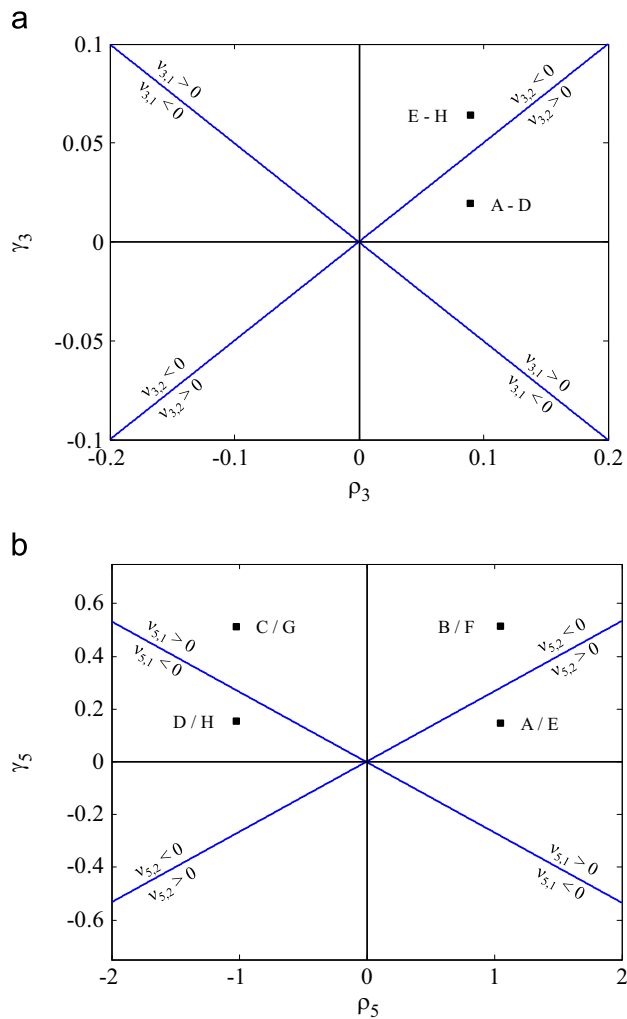
a

b

Fig. 4. (a) Third- and (b) fifth-order non-linear parameter spaces. Note that the labeled data points correspond to the various cases delineated in Table 1, as well as the frequency response plots shown in Figs. 5–12.

Table 1
Parameter values used to produce the frequency response plots shown in Figs. 5–12.

Case	γ_1	ρ_3	γ_3	ρ_5	γ_5
A	0.1	0.1	0.025	1	0.1
B	0.1	0.1	0.025	1	0.5
C	0.1	0.1	0.025	−1	0.5
D	0.1	0.1	0.025	−1	0.1
E	0.1	0.1	0.075	1	0.1
F	0.1	0.1	0.075	1	0.5
G	0.1	0.1	0.075	−1	0.5
H	0.1	0.1	0.075	−1	0.1

response behavior (as limited, of course, by the perturbation technique employed). In particular, selecting the system parameters such that $\nu_{5,1} > 0$ and $\nu_{5,2} > 0$ results in a frequency response with fifth-order hardening characteristics and selecting $\nu_{5,1} < 0$ and $\nu_{5,2} < 0$ renders a frequency response with fifth-order softening characteristics. Likewise, under certain conditions, $\nu_{5,1}$ and $\nu_{5,2}$ can be selected to have opposite signs which leads to frequency responses with 'mixed' non-linear characteristics, wherein the response curves eventually bend away from one another, potentially leading to theoretically globally unbounded responses.

As with the third-order non-linearities, it proves convenient to utilize the upper half-plane of fifth-order non-linear parameter space, shown in Fig. 4(b), in order to characterize the qualitative behavior of the system's global frequency response. As the system behavior within this parameter space, as well as its dependence on AC and DC excitations, is largely akin to that described above in the context of the system's third-order non-linearities, further discussion is omitted.

In order to display each of the qualitatively distinct frequency responses that can be recovered for the equation of motion detailed in Eq. (31), a number of representative cases, detailed in Table 1 and by the data points in Fig. 4, are subsequently considered. Note that while most of these cases are readily obtainable using a given EMA microcantilever design, additional responses have been included for the sake of completeness (largely to assist those working on related problems). Furthermore, note that only those cases in the first quadrant of the third-order parameter space are included. The behavior of resonators operating in the second quadrant, namely those operating with large, negative, DC tuning biases, can be easily determined through symmetry arguments.

The frequency response plots corresponding to data points A–H in Table 1 and Fig. 4 are included in Figs. 5–12. As the majority of the responses highlighted in these figures are qualitatively distinct from one another, each is considered in turn.

The frequency response plot shown in Fig. 5, representative of all systems with $\nu_{3,1} > 0$, $\nu_{3,2} > 0$, $\nu_{5,1} > 0$, and $\nu_{5,2} > 0$ and corresponding to Case A, clearly depicts a classical hardening response. That is, the system's non-trivial response branches both result from pitchfork bifurcations (one supercritical and one subcritical) occurring at σ_1 and σ_2, respectively, and bend to the right, ultimately yielding a globally bounded system response.[5] The response shown in Fig. 6, representative of all systems with $\nu_{3,1} > 0$, $\nu_{3,2} > 0$, $\nu_{5,1} > 0$, and $\nu_{5,2} < 0$ and corresponding to Case B, is slightly more complicated. Here, the response incorporates all of the features detailed above for Case A, but also an additional

To summarize the results outlined above, it proves convenient to utilize the upper half-plane of the third-order non-linear parameter space shown in Fig. 4(a), as identifying the resonator's location with this parameter space allows for the rapid prediction of system's qualitative behavior (at least to third-order).[4] Noting, for example, that the EMA microcantilevers detailed herein initially lie on the positive half of the ρ_3 axis reveals that they, in the absence of excitation, exhibit third-order hardening characteristics. This position is not fixed, however, as adding an AC excitation allows the resonator's location in the third-order parameter space to translate in the vertical direction and thus allows the system's third-order behavior to transition to a mixed response. Likewise, adding a DC excitation allows the oscillator's location to translate in the horizontal direction and thus facilitates transitions to softening or mixed third-order responses.

Though the third-order non-linearities dictate the immediate post-pitchfork-bifurcation behavior of the system, the fifth-order effective non-linearities dictate the system's 'global' frequency

---

(*footnote continued*)
complicated here, however, as one or more constant amplitude solutions is also likely to exist.

[4] Note that the resonators detailed herein are not expected to operate in the lower half-plane of the third-order parameter space, wherein the previously detailed constant-amplitude solution exist.

[5] Note that the term 'globally bounded' is used here, and throughout the remainder of this work, to designate the fact that all initial conditions result in a bounded response.
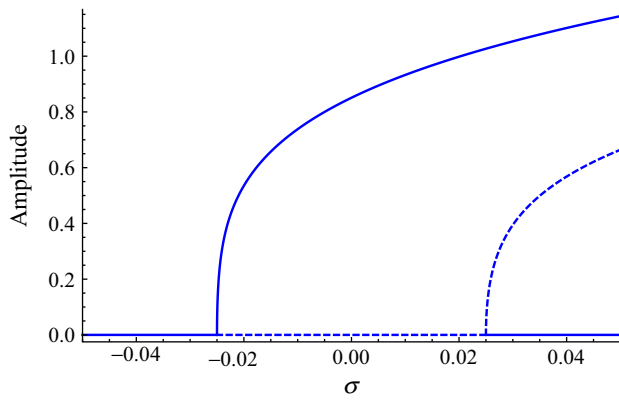
Fig. 5. Frequency response plot corresponding to Case A. Note that here, and throughout the remainder of the work, solid lines on frequency response plots are used to designate stable steady-state solutions, and dashed lines are used to designate unstable steady-state solutions.
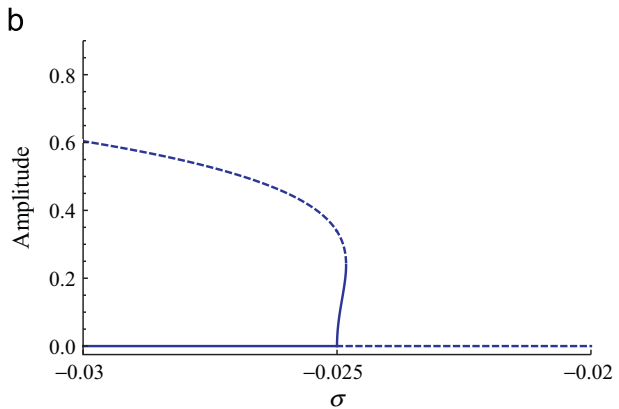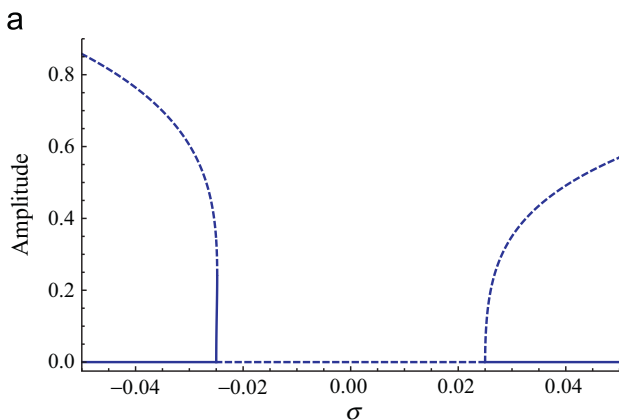

Fig. 7. (a) Frequency response plot corresponding to Case C. (b) A close-up view of the system's frequency response in the proximity of $\sigma = -0.025$.

Fig. 6. (a) Frequency response plot corresponding to Case B. (b) A close-up view of the system's frequency response in the proximity of $\sigma = -0.025$.

Fig. 8. Frequency response plot corresponding to Case D.

saddle-node bifurcation at σ_4. This additional bifurcation point not only leads to a destabilization of the left branch, but also causes the branch to bend to the left yielding a globally unstable system response. Fig. 7, corresponding to Case C, depicts a response qualitatively equivalent to that seen in Case B, despite the fact that the sign of ρ_5 has changed. Though counterintuitive, this is consistent with the system's stated dependence on the fifth-order effective non-linearities, and is thus included only for the sake of completeness. The final frequency response plot realizable for positive values of $\nu_{3,1}$ and $\nu_{3,2}$, designated Case D, is depicted in Fig. 8. Here, due to the fact that both $\nu_{5,1}$ and $\nu_{5,2}$ are negative, each of the system's non-trivial branches undergo saddle-node
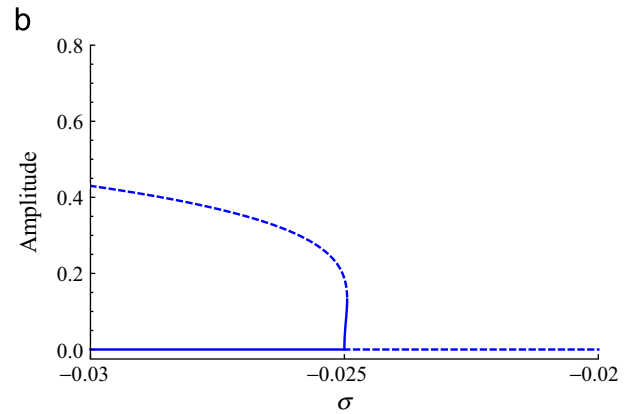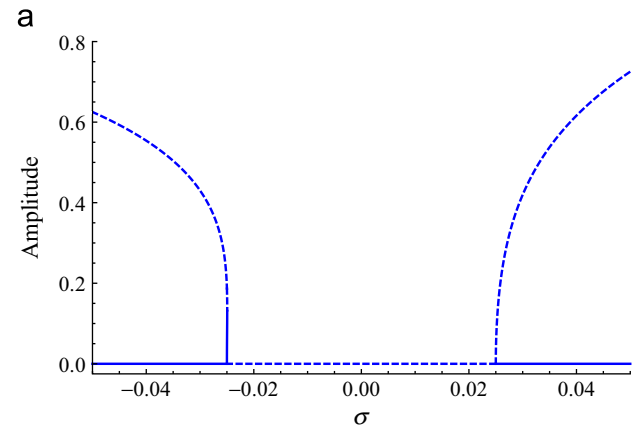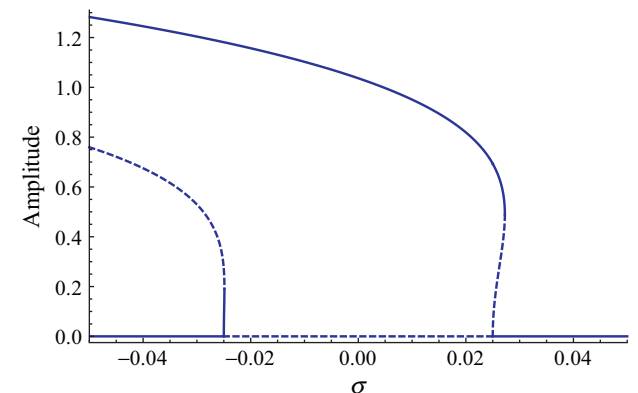
bifurcations, at σ_3 and σ_4 respectively, yielding a globally bounded response wherein both response branches ultimately bend to the left in a softening-like manner.

Figs. 9–12, corresponding to Cases E–H, are representative of systems with mixed third-order non-linearities, that is systems with $\nu_{3,1} > 0$ and $\nu_{3,2} < 0$. The first response in this series, designated Case E and representative of systems with $\nu_{5,1} > 0$ and $\nu_{5,2} > 0$ is shown in Fig. 9. Here, as expected, the system has two non-trivial branches – the result of pitchfork bifurcations at σ_1 and σ_2, respectively – that initially bend away from one another. However, in this case, the left branch undergoes a saddle-node bifurcation at σ_4, which not only stabilizes the branch, but also
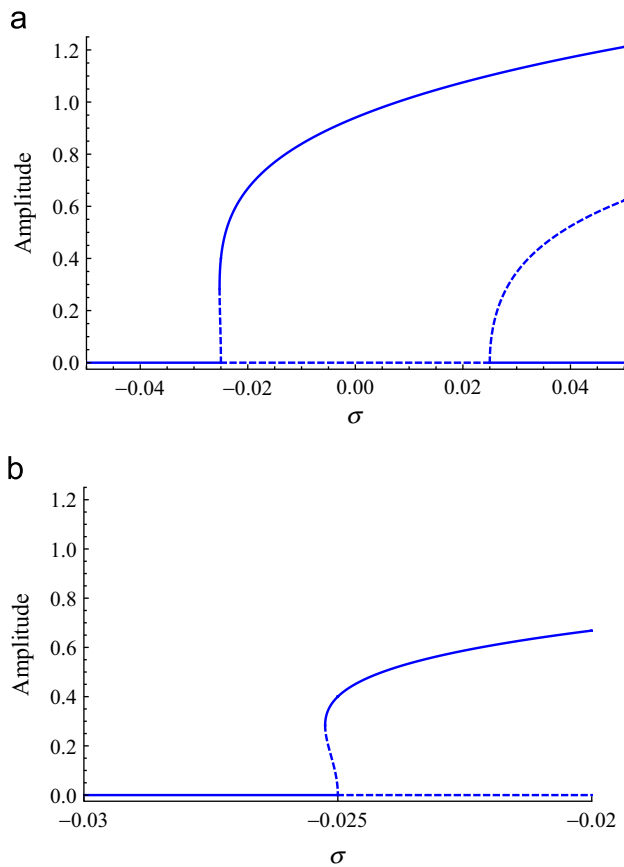
a

b

Fig. 9. (a) Frequency response plot corresponding to Case E. (b) A close-up view of the system's frequency response in the proximity of $\sigma = -0.025$.
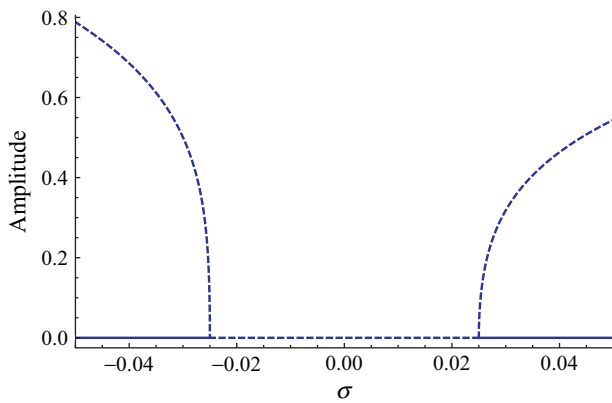

Fig. 10. Frequency response plot corresponding to Case F.

causes it to bend to the right, ultimately yielding a globally stable, hardening-like system response. Figs. 10 and 11, corresponding to Cases F and G, respectively, are representative of systems with $\nu_{5,1} > 0$ and $\nu_{5,2} < 0$. Here, neither of the non-trivial branches undergo additional bifurcations, and thus these branches which initially bend away from each other continue to do so for all values of detuning. The last response in the series, designated Case H and corresponding to systems with $\nu_{5,1} < 0$ and $\nu_{5,2} < 0$ is shown in Fig. 12. Here, as with all responses in this series, the responses branches initially bend away from one another. However, at σ_3 the right branch undergoes a saddle-node bifurcation, which not only stabilizes it, but also causes it to bend to the left, yielding a softening-like response.
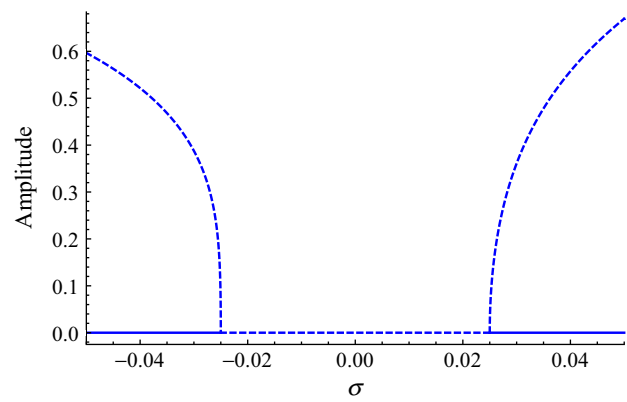

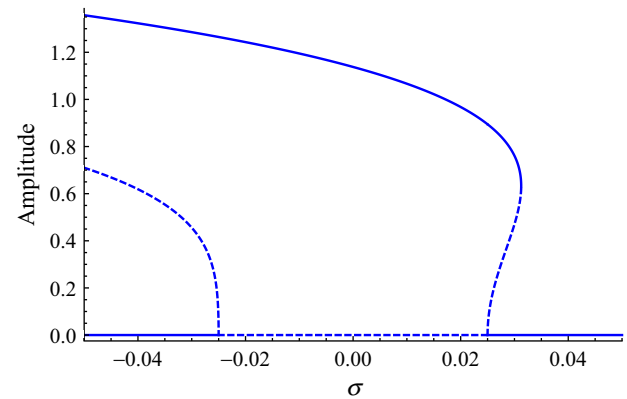**Fig. 11.** Frequency response plot corresponding to Case G.

Fig. 12. Frequency response plot corresponding to Case H.

Table 2
Parameter values, obtained from a representative microcantilever, used to produce Figs. 13–17.

Physical parameter	Value
Width	23.5 μm
Length	162 μm
Thickness	250 nm
Young's modulus (E)	159 GPa
Mass density (ρ)	2330 kg/m^3
Magnetic field strength (B)	1 T

From Figs. 5–12, it is apparent that a wide variety of distinct frequency response structures are obtainable with the system of interest. By properly selecting design parameters and excitation conditions, virtually any point in the third- and the fifth-order parameter spaces (Fig. 4) could be chosen as a device operating point which allows for tunable frequency response structures. Section 7 describes the behavior of a representative microcantilever system and highlights the tunable nature of its response.

7. The response of a representative EMA microbeam system

While the preceding section provides a comprehensive overview of the qualitatively distinct frequency response structures that can be realized with a given electromagnetically actuated microbeam system, it does not clearly delineate how these responses depend on various system parameters and excitation signals. In light of this, the present section examines the frequency response behavior of a representative parametrically excited EMA microbeam (see Table 2 for details). Note that for present purposes, the impedance of the microbeam system is assumed to be
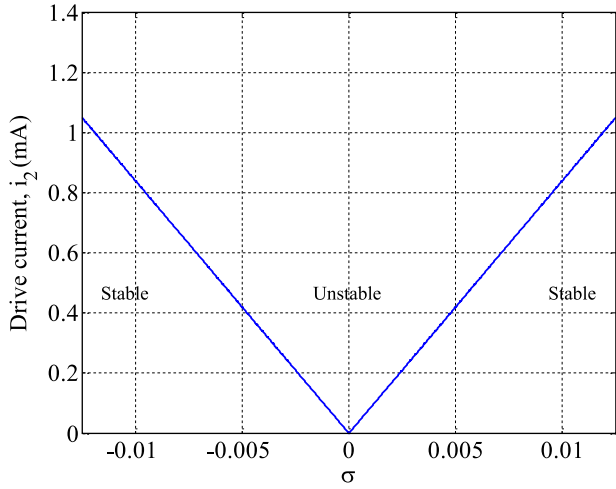
Fig. 13. Linear stability chart showing the transition between the stable and unstable regimes of the trivial solution. Note that in this figure and Figs. 14–17, the parameter values stated in Table 2 are utilized.
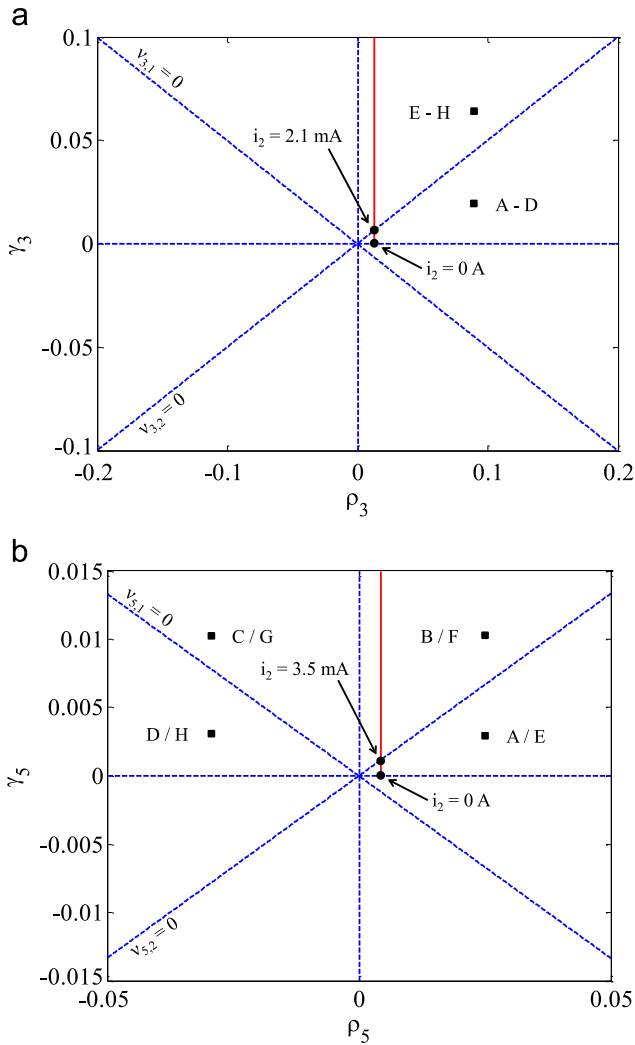

Fig. 14. Sample third-order (a) and fifth-order (b) non-linear parameter spaces corresponding to the representative EMA microbeam system. The figure shows the transition between different parameter regions for $i_{DC}=0$ and an increasing value of i_2. As the drive current i_2 is increased, the system initially undergoes a bifurcation in the third-order space at $\nu_{3,2}=0$ and then a bifurcation in the fifth-order space at $\nu_{5,2}=0$.

of sufficient magnitude that the induced emf does not appreciably impact the system's excitation signal.

Using the results of Section 5, the behavior of the representative microbeam system delineated in Table 2 can be systematically recovered. As this behavior is qualitatively dependent on the magnitudes of i_{DC} and i_2, the present discussion is framed in the context of varying drive currents. Note that the effect of drive current i_2 on the linear, undamped response of the system can be clearly identified from Fig. 13. This figure shows the stability boundaries for the trivial solution as a function of drive current. As the drive current (i_2) increases (which, in turn affects the linear parametric excitation term, γ_1), the width of instability zone increases. The behavior is consistent with a typical Mathieu system. Note that, in practical implementations, viscous damping affects the shape of the instability wedge, by rounding off the bottom of the wedge and setting a threshold value for drive current at which the transition to the unstable region occurs.

Fig. 14 shows the effect of drive current on the non-linear behavior of the system. For a fixed value of the DC offset current, varying the value of i_2 yields purely vertical translations across both the third-order and fifth-order parameter spaces. Starting at $i_2=0$ A, as the current is increased, the first bifurcation occurs in the third-order parameter space ($\nu_{3,2}=0$) at $i_2=2.1$ mA. Increasing i_2 further, the next bifurcation occurs in the fifth-order parameter space ($\nu_{5,2}=0$) at $i_2=3.5$ mA. A change in i_{DC} would yield qualitatively similar behavior, with the horizontal location of the path varying with the value of i_{DC}. Thus, by choosing appropriate values for the drive currents, very distinct behaviors can be obtained with the system.

Fig. 15 depicts the frequency response structure of an electromagnetically actuated microbeam excited with comparatively small drive amplitudes, namely, $i_{DC}=0.0$ mA and $i_2=1.0$ mA. As expected, this operating condition, much like its unforced counterpart, renders a hardening response, similar to Case A, wherein both of the system's non-trivial response branches bend to the right. Increasing the amplitude of the system's AC drive current (i_2) past the first bifurcation at the $\nu_{3,2}=0$ threshold yields the frequency response depicted in Fig. 16, which was produced using drive currents of $i_{DC}=0.0$ mA and $i_2=3.0$ mA. This response, similar to Case E, features hardening-like global behavior, wherein both response branches eventually bend to the right (following an additional saddle node bifurcation on the left non-trivial branch). Further increasing the system's AC drive current (i_2) from this operating point past the bifurcation at the $\nu_{5,2}=0$ threshold, yields the frequency response structure shown in Fig. 17. This response structure was produced using drive currents of $i_{DC}=0.0$ mA and $i_2=4.0$ mA. This response, similar to Case F, features a globally unbounded frequency response, wherein the non-trivial response branches bend away from one
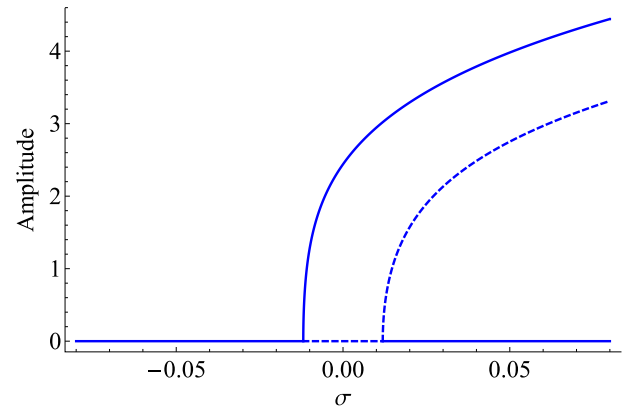

Fig. 15. Frequency response plot corresponding to the representative microbeam system operated with $i_{DC}=0.0$ mA and $i_2=1.0$ mA.
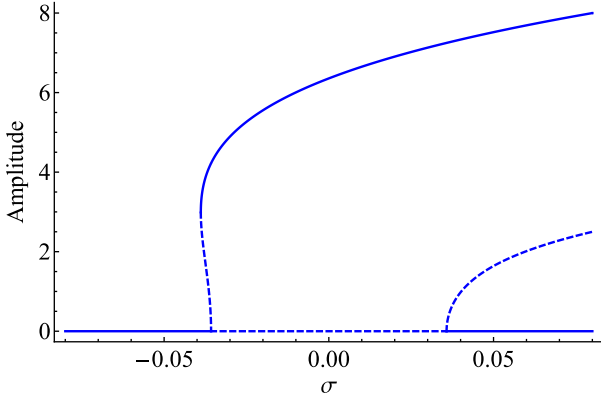
Fig. 16. Frequency response plot corresponding to the representative microbeam system operated with $i_{DC}=0.0$ mA and $i_2=3.0$ mA.
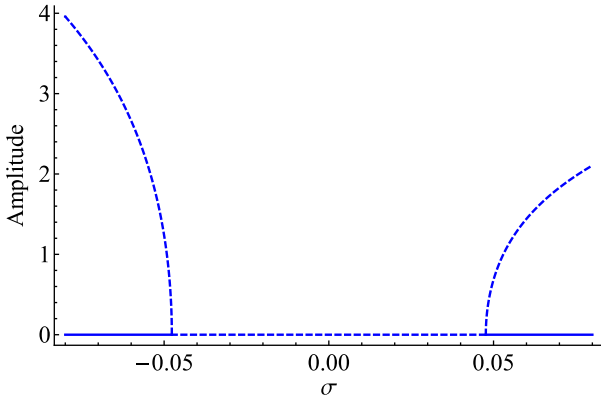

Fig. 17. Frequency response plot corresponding to the representative microbeam system operated with $i_{DC}=0.0$ mA and $i_2=4.0$ mA.

another. Generally speaking, this response, which will undoubtedly be bounded in practice by higher-order non-linearities, is believed to be of limited practical utility.

While the preceding discussion details each of the qualitatively distinct frequency response structures that can be obtained by fixing i_{DC} and varying i_2, it is important to note that the DC bias current can be changed independently or concurrently, as well. This not only allows for linear frequency tuning, but also facilitates the emergence of additional, distinct non-linear frequency response structures. Rather than delineating each of these new structures, of which there are many, here, suffice it to note that a number of qualitatively distinct response can be realized by varying each of the two drive currents provided that the buckling instability and device burnout thresholds are not exceeded.

8. Conclusion

In this work, the non-linear behavior of an electromagnetically actuated microcantilever under purely parametric excitations has been studied. The microcantilever was modeled using energy methods and its frequency response behavior was recovered using the method of averaging. The analysis clearly showed that with careful parameter selection and microcantilever design, a variety of qualitatively distinct responses could be obtained. Building upon these results, ongoing efforts are focused on exploiting the dynamics of electromagnetically actuated arrays of microcantilevers in the design and development of mass sensors and functional oscillator arrays [30].

Appendix A. Dimensionless parameter definitions

$$z = w(\hat{t}) \tag{54}$$

$$\omega_0^2 = \int_0^1 \phi\phi^{iv}d\hat{s} + \frac{i_{DC}gBl^2\cos\alpha}{EI}\int_0^1 \phi'^2\,d\hat{s}$$

$$\int_0^1 \phi^2\,d\hat{s} = 1 \tag{55}$$

$$\tau = \omega_0\hat{t} \tag{56}$$

$$\hat{\omega} = \omega T \tag{57}$$

$$\Omega = \frac{\hat{\omega}}{\omega_0} \tag{58}$$

$$\varepsilon\zeta = \frac{\hat{c}}{2\omega_0} \tag{59}$$

$$\varepsilon\lambda_1 = \frac{i_1gBl^2\cos\alpha}{EI\omega_0^2}\int_0^1 \phi'^2\,d\hat{s} \tag{60}$$

$$\varepsilon\gamma_1 = \frac{i_2gBl^2\cos\alpha}{EI\omega_0^2}\int_0^1 \phi'^2\,d\hat{s} \tag{61}$$

$$\varepsilon\chi_3 = \frac{v_0^2}{\omega_0^2l^2}\int_0^1 \phi\phi''^3d\hat{s} + \frac{4v_0^2}{\omega_0^2l^2}\int_0^1 \phi\phi'\phi''\phi'''d\hat{s} + \frac{v_0^2}{\omega_0^2l^2}\int_0^1 \phi\phi'^2\phi^{iv}\,d\hat{s}$$
$$+ \frac{v_0^2i_{DC}gB\cos\alpha}{2EI\omega_0^2}\int_0^1 \phi'^4\,d\hat{s} \tag{62}$$

$$\varepsilon\chi_5 = \frac{6v_0^4}{\omega_0^2l^4}\int_0^1 \phi\phi'^2\phi''^3\,d\hat{s} + \frac{8v_0^4}{\omega_0^2l^4}\int_0^1 \phi\phi'^3\phi''\phi'''\,d\hat{s}$$
$$+ \frac{v_0^4}{\omega_0^2l^4}\int_0^1 \phi\phi'^4\phi^{iv}\,d\hat{s}$$
$$+ \frac{3v_0^4i_{DC}gB\cos\alpha}{8EIl^2\omega_0^2}\phi'^6\,d\hat{s} \tag{63}$$

$$\varepsilon\lambda = \frac{i_1v_0^2gB\cos\alpha}{2EI\omega_0^2}\int_0^1 \phi'^4\,d\hat{s} \tag{64}$$

$$\varepsilon\gamma_3 = \frac{i_2v_0^2gB\cos\alpha}{2EI\omega_0^2}\int_0^1 \phi'^4\,d\hat{s} \tag{65}$$

$$\varepsilon\lambda_5 = \frac{3i_1v_0^4gB\cos\alpha}{8EIl^2\omega_0^2}\int_0^1 \phi'^6\,d\hat{s} \tag{66}$$

$$\varepsilon\gamma_5 = \frac{3i_2v_0^4gB\cos\alpha}{8EIl^2\omega_0^2}\int_0^1 \phi'^6\,d\hat{s} \tag{67}$$

$$\varepsilon\beta = \frac{v_0^2}{l^2}\int_0^1 \phi\phi''\int_1^{\hat{s}}\int_0^{\hat{s}} \phi'^2\,d\hat{s}\,d\hat{s}\,d\hat{s} + \frac{v_0^2}{l^2}\int_0^1 \phi\phi'\int_0^{\hat{s}} \phi'^2\,d\hat{s}\,d\hat{s} \tag{68}$$

$$\varepsilon\nu_1 = \frac{3v_0^4}{2l^4}\int_0^1 \phi\phi''\int_1^{\hat{s}}\int_0^{\hat{s}} \phi'^4\,d\hat{s}\,d\hat{s}\,d\hat{s} + \frac{3v_0^4}{2l^4}\int_0^1 \phi\phi'\int_0^{\hat{s}} \phi'^4\,d\hat{s}\,d\hat{s}$$
$$+ \frac{3v_0^4}{2l^4}\int_0^1 \phi\phi'^2\phi''\int_1^{\hat{s}}\int_0^{\hat{s}} \phi'^2\,d\hat{s}\,d\hat{s}\,d\hat{s} + \frac{v_0^4}{2l^4}\int_0^1 \phi\phi'^3\int_0^{\hat{s}} \phi'^2\,d\hat{s}\,d\hat{s} \tag{69}$$

$$\varepsilon\nu_2 = \frac{v_0^4}{2l^4} \int_0^1 \phi\phi'' \int_1^{\hat{s}} \int_0^{\hat{s}} \phi'^4 \, d\hat{s} \, d\hat{s} \, d\hat{s} + \frac{v_0^4}{2l^4} \int_0^1 \phi\phi' \int_0^{\hat{s}} \phi'^4 \, d\hat{s} \, d\hat{s}$$
$$+ \frac{3v_0^4}{2l^4} \int_0^1 \phi\phi'^2\phi'' \int_1^{\hat{s}} \int_0^{\hat{s}} \phi'^2 \, d\hat{s} \, d\hat{s} \, d\hat{s} + \frac{v_0^4}{2l^4} \int_0^1 \phi\phi'^3 \int_0^{\hat{s}} \phi'^2 \, d\hat{s} \, d\hat{s}$$

$$(70)$$

$$\varepsilon\eta_0 = \frac{i_{DC}gBl^3 \sin\alpha}{EIv_0\omega_0^2} \phi(1) \qquad (71)$$

$$\varepsilon\eta_1 = \frac{i_1gBl^3 \sin\alpha}{EIv_0\omega_0^2} \phi(1) \qquad (72)$$

$$\varepsilon\eta_2 = \frac{i_2gBl^3 \sin\alpha}{EIv_0\omega_0^2} \phi(1) \qquad (73)$$

References

[1] A.N. Cleland, M.L. Roukes, Fabrication of high frequency nanometer scale mechanical resonators from bulk Si crystals, Applied Physics Letters 69 (18) (1996) 2653–2655.

[2] O. Cugat, J. Delamare, G. Reyne, Magnetic micro-actuators and systems (MAGMAS), IEEE Transactions on Magnetics 39 (5) (2003) 3607–3612.

[3] A.N. Cleland, Foundations of Nanomechanics: From Solid-State Theory to Device Applications, Advanced Texts in Physics, Springer, Berlin, 2003.

[4] S.C. Jun, X.M.H. Huang, J. Hone, C.A. Zorman, M. Mehregany, Evaluation of 3C–SiC nanomechanical resonators using room temperature magnetomotive transduction, in: Proceedings of IEEE Sensors 2005: The 4th IEEE Conference on Sensors, Irvine, California, 2005, pp. 1042–1045.

[5] A. Husain, J. Hone, H.W.C. Postma, X.M.H. Huang, T. Drake, M. Barbic, A. Scherer, M.L. Roukes, Nanowire-based very-high-frequency electromechanical resonator, Applied Physics Letters 83 (6) (2003) 1240–1242.

[6] D.S. Greywall, Micromechanical RF filters excited by the Lorentz force, Journal of Micromechanics and Microengineering 9 (1) (1999) 78–84.

[7] A.N. Cleland, M.L. Roukes, A nanometer-scale mechanical electrometer, Nature 392 (6672) (1998) 160–162.

[8] D. Golda, M.L. Culpepper, Two-axis electromagnetic moving-coil micro-actuator, in: Proceedings of IMECE 2006: The 2006 ASME International Mechanical Engineering Conference and Exposition, Chicago, Illinois, 2006.

[9] H.-K. Lee, K.-S. Kim, E. Yoon, A wide-ranging linearly tunable optical filter using Lorentz force, IEEE Photonics Technology Letters 16 (9) (2004) 2087–2089.

[10] T. Kemp, M. Ward, Tunable response nano-mechanical beam resonator, Sensors and Actuators A: Physical 123–124 (2005) 281–284.

[11] S.J. Martin, M.A. Butler, J.J. Spates, M.A. Mitchell, W.K. Schubert, Flexural plate wave resonator excited with Lorentz forces, Journal of Applied Physics 83 (9) (1998) 4589–4601.

[12] X.M.H. Huang, X.L. Feng, C.A. Zorman, M. Mehregany, M.L. Roukes, VHF, UHF and microwave frequency nanomechanical resonators, New Journal of Physics 7 (247) (2005) 1–15.

[13] X.M.H. Huang, M. Manolidis, S.C. Jun, J. Hone, Nanomechanical hydrogen sensing, Applied Physics Letters 86 (14) (2005) 143104.

[14] M. Schiffer, V. Laible, E. Obermeier, Design and fabrication of 2D Lorentz force actuated micromirrors, in: Proceedings of the 2002 IEEE/LEOS International Conference on Optical MEMS, Lugano, Switzerland, 2002, pp. 163–164.

[15] M.J. Thompson, D.A. Horsley, Parametrically amplified z-axis Lorentz force magnetometer, Journal of Microelectromechanical Systems 20 (3) (2011) 702–710.

[16] M.V. Requa, Parametric Resonance in Microcantilevers for Applications in Mass Sensing, Ph.D. Dissertation, University of California, 2006.

[17] M.V. Requa, K.L. Turner, Electromechanically driven and sensed parametric resonance in silicon microcantilevers, Applied Physics Letters 88 (26) (2006) 263508.

[18] M.V. Requa, K.L. Turner, Precise frequency estimation in a microelectromechanical parametric resonator, Applied Physics Letters 90 (17) (2007) 173508.

[19] J.F. Rhoads, Exploring and Exploiting Resonance in Coupled and/or Nonlinear Microelectromechanical Oscillators, Ph.D. Dissertation, Michigan State University, 2007.

[20] W. Zhang, F. Wang, M. Yao, Global bifurcations and chaotic dynamics in nonlinear nonplanar oscillations of a parametrically excited cantilever beam, Nonlinear Dynamics 40 (3) (2005) 251–279.

[21] N. Kacem, S. Hentz, D. Pinto, B. Reig, V. Nguyen, Nonlinear dynamics of nanomechanical beam resonators: improving the performance of NEMS-based sensors, Nanotechnology 20 (27) (2009) 275501.

[22] J.F. Rhoads, S.W. Shaw, K.L. Turner, Nonlinear dynamics and its applications in micro- and nanoresonators, Journal of Dynamic Systems, Measurement, and Control 132 (3) (2010) 034001.

[23] M.R.M. Crespo da Silva, C.C. Glynn, Nonlinear flexural-flexural-torsional dynamics of in extensional beams. I: equations of motion, Journal of Structural Mechanics 6 (4) (1978) 437–448.

[24] M.R.M. Crespo da Silva, C.C. Glynn, Nonlinear flexural-flexural-torsional dynamics of inextensional beams. II: forced motions, Journal of Structural Mechanics 6 (4) (1978) 449–461.

[25] P. Malatkar, Nonlinear Vibrations of Cantilever Beams and Plates, Ph.D. Dissertation, Virginia Polytechnic Institute and State University, 2003.

[26] J.F. Rhoads, S.W. Shaw, K.L. Turner, The nonlinear response of resonant microbeam systems with purely-parametric electrostatic actuation, Journal of Micromechanics and Microengineering 16 (5) (2006) 890–899.

[27] J.F. Rhoads, S.W. Shaw, K.L. Turner, R. Baskaran, Tunable microelectromechanical filters that exploit parametric resonance, Journal of Vibration and Acoustics 127 (5) (2005) 423–430.

[28] J.F. Rhoads, S.W. Shaw, K.L. Turner, J. Moehlis, B.E. DeMartini, W. Zhang, Generalized parametric resonance in electrostatically actuated microelectromechanical oscillators, Journal of Sound and Vibration 296 (4–5) (2006) 797–829.

[29] S.H. Strogatz, Nonlinear Dynamics and Chaos with Applications to Physics, Biology, Chemistry, and Engineering, Westview, Cambridge, 1994.

[30] V. Kumar, A. Sabater, J.F. Rhoads, Dynamics of coupled electromagnetically-actuated microbeams, in: Proceedings of the 2011 NSF Engineering Research and Innovation Conference, Atlanta, Georgia, 2011.